8-1-2005

Theoretical Investigation of Electroosmotic Flows and Chaotic Stirring in Rectangular Cavities

Shizhi Qian
University of Pennsylvania

Haim H. Bau
University of Pennsylvania, bau@seas.upenn.edu

Postprint version. Published in *Applied Mathematical Modelling*, Volume 29, Issue 8, August 2005, pages 726-753.
Publisher URL: http://dx.doi.org/10.1016/j.apm.2004.10.006

Theoretical Investigation of Electroosmotic Flows and Chaotic Stirring in Rectangular Cavities

Abstract

Two dimensional, time-independent and time-dependent electro-osmotic flows driven by a uniform electric field in a closed rectangular cavity with uniform and nonuniform zeta potential distributions along the cavity's walls are investigated theoretically. First, we derive an expression for the one-dimensional velocity and pressure profiles for a flow in a slender cavity with uniform (albeit possibly different) zeta potentials at its top and bottom walls. Subsequently, using the method of superposition, we compute the flow in a finite length cavity whose upper and lower walls are subjected to non-uniform zeta potentials. Although the solutions are in the form of infinite series, with appropriate modifications, the series converge rapidly, allowing one to compute the flow fields accurately while maintaining only a few terms in the series. Finally, we demonstrate that by time-wise periodic modulation of the zeta potential, one can induce chaotic advection in the cavity. Such chaotic flows can be used to stir and mix fluids. Since devices operating on this principle do not require any moving parts, they may be particularly suitable for microfluidic devices.

Keywords

Electrosmosis, chaos, stirring, microfluidics, mixing, stokes flow, accelerated convergence, Meleshko

Comments

Postprint version. Published in *Applied Mathematical Modelling*, Volume 29, Issue 8, August 2005, pages 726-753.

Publisher URL: http://dx.doi.org/10.1016/j.apm.2004.10.006

Citation information: Qian, S. and Bau, H., H., 2005, Theoretical Investigation of Electroosmotic Flows and Chaotic Stirring in Rectangular Cavities, Applied Mathematical Modeling, 29 (8), 726-753.

Theoretical Investigation of Electroosmotic Flows and Chaotic Stirring in Rectangular Cavities

Shizhi Qian and Haim H. Bau*

Department of Mechanical Engineering and Applied Mechanics
University of Pennsylvania, Philadelphia, PA 19104-6315

ABSTRACT

Two dimensional, time-independent and time-dependent electro-osmotic flows driven by a uniform electric field in a closed rectangular cavity with uniform and nonuniform zeta potential distributions along the cavity's walls are investigated theoretically. First, we derive an expression for the one-dimensional velocity and pressure profiles for a flow in a slender cavity with uniform (albeit possibly different) zeta potentials at its top and bottom walls. Subsequently, using the method of superposition, we compute the flow in a finite length cavity whose upper and lower walls are subjected to non-uniform zeta potentials. Although the solutions are in the form of infinite series, with appropriate modifications, the series converge rapidly, allowing one to compute the flow fields accurately while maintaining only a few terms in the series. Finally, we demonstrate that by time-wise periodic modulation of the zeta potential, one can induce chaotic advection in the cavity. Such chaotic flows can be used to stir and mix fluids. Since devices operating on this principle do not require any moving parts, they may be particularly suitable for microfluidic devices.

* To whom all correspondence should be addressed: bau@seas.upenn.edu

1. INTRODUCTION

In recent years, there has been a growing interest in developing microfluidic systems for biological and chemical minute laboratories [1-3]. Often it is necessary to propel fluids from one part of the device to another, control fluid motion, enhance mixing, and separate fluids. Electro-osmosis provides an attractive means for manipulating liquids in microdevices. The electro-osmotic phenomenon is caused by the accumulation of a net electric charge on the solid's surface that is in contact with an electrolyte solution. As a result, counterions accumulate in a thin liquid layer next to the solid's surface. This thin layer is known as the Debye (or double) layer, and its thickness is typically on the order of 10nm [4]. Away from the solid's surface, the electrolyte is neutral. This charge separation next to the solid wall causes either a positive or negative (ζ) potential difference across the Debye layer. The magnitude of the ζ potential depends, among other things, on the characteristics of the solid and the liquid. In the presence of an external electric field, the counterions in the double layer are attracted to the oppositely charged electrode and drag the liquid along. In other words, the electric field, through its action on the counterions, creates a body force that, in turn, induces fluid motion. When the Debye layer is much smaller than the conduit's dimensions, the electroosmotic flow can be described by specifying a slip velocity at the wall.

Most of the studies to date have focused on electro-osmotic flows in straight conduits with uniform ζ potential along the conduit's walls. See, for example, Dutta and Beskok [5] and the references cited therein. Just a few studies have addressed electro-osmotic flows in the presence of non-uniform zeta potentials. Assuming a harmonically varying, axi-symmetric zeta potential, Anderson and Idol [6] predicted the occurrence of secondary flows and showed that the average, axial electro-osmotic velocity is proportional to the axial average of the zeta

potential. Ajdari [7-9] studied complex electro-osmotic flows induced by non-uniform, time-independent and time-dependent ζ potentials along the conduit's walls. Qian and Bau [10] studied electro-osmotic flows in an infinite conduit whose wall potential was actively controlled spatially and temporally. They demonstrated that by alternating between two different flow fields, one could induce Lagrangian chaos that facilitates effective stirring. Erickson and Li [11] used surface heterogeneity to enhance mixing in a T-shaped microchannel.

Nonuniform ζ potentials can be obtained by coating the conduit's walls with different materials [12] or by using different buffer solutions. More interestingly, both spatial and temporal control of the ζ potential can be achieved by imposing an electric field perpendicular to the solid-liquid interface [13-15]. Such a normal electric field can be imposed with the aid of electrodes embedded beneath the solid-liquid interface and electrically insulated from the liquid. Alternatively, when the solid surface is photosensitive (such as a semi-conducting TiO_2 film), the surface charge can be modified with light [16].

In this paper, we study electroosmotic flows in rectangular cavities with nonuniform ζ potentials along the cavity's walls. The calculation of the flow field requires the solution of the Stokes problem. Using the superposition method, we derive expressions for the flow field in the form of infinite series. Unfortunately, the resulting series converge slowly. Using various acceleration techniques [17], we recast the series in a fast converging form and demonstrate that just a few terms are sufficient to obtain highly accurate results. These series solutions are far superior both in precision and computational time to finite difference or finite elements solutions [18] when one desires to track the trajectories of passive tracers. The paper is organized as follows. We first set up the mathematical model (section 2), and then we review the results for one-dimensional flow driven by both electro-osmosis and the pressure gradient between two

plates that are parallel to the imposed electric field (section 3). Subsequently, using boundary layer analysis and asymptotic matching, we reproduce the well-known result that the core flow can be computed using slip boundary conditions at the walls (section 4). It appears, however, that rigorous matching of the core and boundary layer solutions has not previously been carried out. The boundary layer analysis reveals the presence of additional terms in the "inner solution" that corresponds to the pressure gradient's effect on the wall shear stress. In section 5, we obtain the velocity profile in a slender, closed cavity far from the sidewalls. This solution will aid us later in verifying the calculations of the flow field in a finite aspect ratio cavity. In section 6, we compute two-dimensional electro-osmotic flows in rectangular cavities with finite aspect ratios and with various distributions of the ζ potential along the cavities' boundaries. Finally, following ideas promoted by Aref [19], we alternate periodically between two different flow fields and demonstrate that one can induce chaotic advection in the cavity. The ability of such chaotic flows to stir the fluid is demonstrated by following the advection of passive tracer particles. Since the stirrer does not require any moving parts, it may be useful for stirring liquids in micro fluidic devices.

2. MATHEMATICAL MODEL

Consider the closed cavity $|x| \leq L$ and $|y| \leq H$ depicted in Fig. 1. The two electrodes mounted along the walls $x = \pm L$ induce an electric field $\vec{E}_x$ parallel to the x-axis. Additional electrodes (A_i) are embedded in the cavity's upper and lower walls. These electrodes are not in contact with the liquid, and they are used to control the ζ potential at the liquid-solid interface [14]. The cavity contains an electrolytic solution. We assume that the salt in the solution is fully dissociated and consists of equal numbers of positive and negative ions:

$$z^+ = -z^- = z\,. \tag{2.1}$$

As a result of the interaction of the ionized solution with the static charges on the solid walls, a thin electric double (Debye) layer is formed next to the solid walls [4]. The motion of the ionized, incompressible fluid with electro-osmotic body forces is governed by the incompressible Navier-Stokes equation,

$$\rho_f \frac{D\vec{V}^*}{Dt} = -\nabla \hat{p}^* + \mu \nabla^2 \vec{V}^* + \rho_e \vec{E}\,, \tag{2.2}$$

and the continuity equation,

$$\nabla \bullet \vec{V}^* = 0\,. \tag{2.3}$$

In the above, $\hat{p}^*$ is the pressure, $\vec{V}^*$=(u*, v*) is the velocity vector, u* and v* are, respectively, the velocity components in the x and y directions, ρ_f is the fluid density, and ρ_e is the net electric charge density.

We decompose the electric potential in the cavity into two components: $\Phi(x) + \phi(x, y)$. Φ satisfies Laplace's equation, $\nabla^2 \Phi = 0$, with $\left(\frac{\partial \Phi}{\partial y}\right)_{y=\pm H} = 0$. ϕ satisfies the Poisson-Boltzmann equation [4,20],

$$\nabla^2 \phi = -\frac{\rho_e}{\varepsilon} = -\frac{Fz}{\varepsilon}(c^+ - c^-) = \frac{2Fzc_0}{\varepsilon} \sinh\left(\frac{Fz\,\phi}{RT}\right), \tag{2.4}$$

where ε is liquid's permittivity; ρ_e is the net charge density; F is Faraday constant, and c^+ and c^- are, respectively, the concentrations of the positive and negative ions that satisfy the Boltzmann distribution.

Next, we rewrite the momentum equation as

$$\rho_f \frac{D\vec{V}^*}{Dt} = -\nabla p^* + \mu \nabla^2 \vec{V}^* - \varepsilon \nabla^2 \phi\, E_x\,, \tag{2.5}$$

where $E_x = -\nabla\Phi$, $p^* = \hat{p}^* - q$, and $q = 2c_0 RT\cosh\left(\frac{Fz\phi}{RT}\right)$.

Using $\frac{RT}{Fz}$ and H as the potential and length scales, respectively, we define $\hat{\chi} = \frac{Fz\phi}{RT}$ and $Y = \frac{y}{H}$. Furthermore, assuming that next to the solid liquid interface, $\frac{\partial\hat{\chi}}{\partial x} << \frac{\partial\hat{\chi}}{\partial y}$, equation 2.4 is simplified to

$$\lambda_D{}^2 \frac{\partial^2\hat{\chi}}{\partial Y^2} = \sinh\hat{\chi}, \tag{2.6}$$

where $\lambda_D = \frac{\lambda_D^*}{H}$ and $\lambda_D^* = \sqrt{\frac{RT\varepsilon}{2F^2z^2c_o}}$ are, respectively, the dimensionless and dimensional thickness of the Debye layer. Typically, λ_D^* is on the order of 10nm and $\lambda_D << 1$. Consequently, we can separate the domain into three regions: upper layer (denoted with a subscript +), lower layer (denoted with subscript -), and a core (neutral) layer. In the core, $\hat{\chi} = \frac{\partial\hat{\chi}}{\partial Y} = 0$.

Upon integrating equation (2.6) twice, taking advantage of the smallness of λ_D, and superposing the solutions for the upper and lower layers, we obtain:

$$\hat{\chi}(Y) \approx 4\tanh^{-1}\left[\tanh\left(\frac{\zeta_+}{4}\right)\exp\left(-\frac{1-Y}{\lambda_D}\right)\right] + 4\tanh^{-1}\left[\tanh\left(\frac{\zeta_-}{4}\right)\exp\left(-\frac{1+Y}{\lambda_D}\right)\right] \tag{2.7}$$

In the above, the first and second terms correspond, respectively, to the potential distribution in the vicinity of the upper and lower walls. ζ_+ and ζ_- denote, respectively, the dimensionless zeta potentials at the upper (+) and lower (-) walls. When $\chi << 1$, $\tanh\chi \approx \chi$ (the Debye-Hückel linearization), and (2.7) can be further simplified to

$$\hat{\chi}(Y) \approx \zeta_+\exp\left(-\frac{1-Y}{\lambda_D}\right) + \zeta_-\exp\left(-\frac{1+Y}{\lambda_D}\right). \tag{2.8}$$

Finally, we re-write the momentum equation (2.5) in dimensionless form. We use, respectively, $-\frac{\varepsilon E_x \left(\phi_+\right)_{\max}}{\mu}$ and $-\frac{\varepsilon E_x (\phi_+)_{\max}}{H}$ as the velocity and pressure scales. The (-) sign in the velocity scale is introduced because when the zeta potential is positive, negative charges are in excess next to the wall, and the fluid in the double layer is driven in a direction opposite to E_x. $\phi_\pm(x)$ is the dimensional zeta potentials. We re-scale $\hat{\chi}$ with $(\zeta_+)_{\max}$ (i.e, $\chi = \frac{\hat{\chi}}{(\zeta_+)_{\max}}$), and assume that $(\zeta_+)_{\max} \neq 0$. The modulation period T (to be introduced later) serves as the time scale. Accordingly, equation (2.5) becomes

$$St^2 \frac{\partial \vec{V}}{\partial t} = -\nabla p + \nabla^2 \vec{V} + \left(\nabla^2 \chi\right)\hat{e}_x \tag{2.9}$$

In the above, $St = \frac{H}{\sqrt{\nu T}}$ is the Stanton number and $\vec{V} = \{U, V\}$ is the dimensionless velocity vector. We also eliminated the advection term since typically electro-osmotic flows are very slow (on the order of μm/s).

3. STEADY ELECTRO-OSMOTIC FLOW IN AN OPEN CONDUIT

In this section, we analyze briefly fully developed, steady electro-osmotic flows in an open, planar conduit with uniform ζ potentials at its top and bottom walls. Later, we will use this solution to construct the flow field far from the sidewalls in a closed, slender cavity. To this end, we solve the x-direction momentum equation (2.9) with the boundary conditions

$$U(\pm 1) = 0 \text{ and } \chi(\pm 1) = \zeta_\pm, \tag{3.1}$$

where in our dimensionless scheme $\zeta_+=1$ and $\zeta_-=\alpha$. The velocity profile is:

$$U(Y) = -\left[\chi(Y) + \frac{(\alpha - 1)}{2} Y - \frac{(\alpha + 1)}{2}\right] + \frac{Y^2 - 1}{2} \frac{dP}{dX}. \qquad (3.2)$$

An approximate expression for $\chi(Y)$ is given in equation (2.8).

Fig. 2 depicts the velocity profiles for various pressure gradients and λ_D=0.01 when α=1 (Fig.2a) and α= -1 (Fig.2b). Witness the presence of very thin boundary layers next to the sidewalls (Y=±1). Within the boundary layers, the magnitude of the velocity drops quickly from its "core value" to a zero value at the solid surface. When $\frac{dP}{dX} = 0$ and α=1, the flow is "plug"-like. The cases of $\frac{dP}{dX} < 0$ and $\frac{dP}{dX} > 0$ correspond, respectively, to flows with favorable and adverse pressure gradients. Fig.3 depicts the velocity profiles for different zeta potential ratios with favorable ($\frac{dP}{dX} = -2$, Fig. 3a) and adverse ($\frac{dP}{dX} = 2$, Fig. 3b) pressure gradients. Aside from thin layers next to the walls, the velocity profiles are reminiscent of pressure driven flow between two moving, parallel plates.

4. BOUNDARY LAYER ANALYSIS OF THE FULLY DEVELOPED FLOW IN AN OPEN CONDUIT

As long as the Debye layer is very thin, for all practical purposes, one can replace the non-slip boundary condition at the wall with a "slip velocity " at the edge of the boundary layer [21]. This approximation provides a great simplification when one is computing complex flow fields since it eliminates the need to resolve the velocity field over vastly different length scales. Since later in the paper, we will be using the slip velocity as a boundary condition, we formally justify its use here.

Since χ decays rapidly away from the boundaries, we divide the domain into a core region and two boundary layers. The core variables will be denoted with superscript (c) and the boundary layers variables will be denoted with +/-. In the core region, the dimensionless momentum equation reduces to

$$\frac{\partial^2 U^c}{\partial Y^2} = \frac{dP}{dX}. \tag{4.1}$$

Integrating (4.1) twice with respect to Y, we get

$$U^c(Y) = \frac{1}{2}\frac{dP}{dX}Y^2 + C_2 Y + C_3. \tag{4.2}$$

In the upper and lower boundary layers, we introduce the stretched coordinates $\xi_\pm = \frac{1 \mp Y}{\lambda_D}$.

Rewriting equations 2.8 and 3.2 in terms of the boundary layer variables, we have

$$\chi(\xi_\pm) = \zeta_\pm \exp(-\xi_\pm) \tag{4.3}$$

and

$$U^\pm(\xi_\pm) = \frac{\zeta_\pm}{\zeta_+}\left[1 - \exp(-\xi_\pm)\right] + \frac{{\lambda_D}^2}{2}\frac{dP}{dX}\xi_\pm^2 + C_4^\pm \xi_\pm. \tag{4.4}$$

The coefficients C_2, C_3, and $C_4^\pm$ are obtained by matching the core and the boundary layer solutions. We assume the presence of an overlap region [22] and introduce the "intermediate" variables $\eta^\pm = \frac{1 \mp Y}{\nu}$. $\nu(\lambda_D)$ and $\eta^\pm(\lambda_D)$ are chosen so that $\lim_{\lambda_D \to 0} \frac{\lambda_D}{\nu(\lambda_D)} = 0$ and $\lim_{\lambda_D \to 0} \frac{\lambda_D}{\eta^\pm(\lambda_D)} = 0$. Accordingly, $\xi^\pm = \frac{\nu \eta^\pm}{\lambda_D}$, and $Y = 1 - \nu\eta^+ = \nu\eta^- - 1$.

Asymptotically matching the solutions for various powers of ν, we require:

$$\lim_{\lambda_D \to 0} \frac{U^c - U^+}{\nu^n} = \lim_{\lambda_D \to 0} \frac{1}{\nu^n} \left\{ \left[\frac{1}{2} \frac{dP}{dX} (1 - \nu\eta^+)^2 + C_2 (1 - \nu\eta^+) + C_3 \right] - \left[1 - \exp\left(- \frac{\nu\eta^+}{\lambda_D} \right) + \frac{{\lambda_D}^2}{2} \frac{dP}{dX} \left(\frac{\nu\eta^+}{\lambda_D} \right)^2 + C_4^+ \left(\frac{\nu\eta^+}{\lambda_D} \right) \right] \right\} = 0 \tag{4.5}$$

and

$$\lim_{\lambda_D \to 0} \frac{U^c - U^-}{\nu^n} = \lim_{\lambda_D \to 0} \frac{1}{\nu^n} \left\{ \left[\frac{1}{2} \frac{dP}{dX} (\nu\eta^- - 1)^2 + C_2 (\nu\eta^- - 1) + C_3 \right] - \left[\alpha - \alpha \exp\left(- \frac{\nu\eta^-}{\lambda_D} \right) + \frac{{\lambda_D}^2}{2} \frac{dP}{dX} \left(\frac{\nu\eta^-}{\lambda_D} \right)^2 + C_4^- \left(\frac{\nu\eta^-}{\lambda_D} \right) \right] \right\} = 0 \tag{4.6}$$

To obtain matching for all orders of ν, $C_4^{\pm}$ must be on the order of (λ_D),

$$C_2 = \frac{1 - \alpha}{2}, \quad C_3 = \frac{1 + \alpha}{2} - \frac{1}{2} \frac{dP}{dX}, \text{ and } C_4^{\pm} = \mp \lambda_D \left(\frac{1 - \alpha}{2} \pm \frac{dP}{dX} \right).$$

Consequently,

$$U^c(Y) = \frac{1}{2} \frac{dP}{dX} (Y^2 - 1) + \frac{1 - \alpha}{2} Y + \frac{1 + \alpha}{2} \tag{4.7}$$

$$U^{\pm}(\xi_{\pm}) = \frac{\zeta_{\pm}}{\zeta_+} \left[1 - \exp(-\xi_{\pm}) \right] + \frac{{\lambda_D}^2}{2} \frac{dP}{dX} \xi_{\pm}^2 \mp \lambda_D \left(\frac{1 - \alpha}{2} \pm \frac{dP}{dX} \right) \xi_{\pm} \tag{4.8}$$

Although the pressure gradient enters into the order of λ_D in the boundary layer equation, it provides *0*(1) contribution to the wall shear stress. Not surprisingly, even in the presence of pressure gradients, the core solution can be completely resolved by assuming slip boundary conditions at the walls $U^c(1)=1$ and $U^c(-1)=\alpha$.

5. STEADY ELECTRO-OSMOTIC FLOW IN A SLENDER, CLOSED CAVITY

When the cavity is closed, the pressure gradient is no longer independent, and mass conservation requires

$$\int_{-1}^{1} U\ (Y)\,dY\ =\ 0\ . \tag{5.1}$$

In the case of a slender cavity, H/L<<1, and far from the side walls, one may assume that $\frac{\partial U}{\partial X} = 0$. Substituting (3.2) into (5.1), we obtain

$$\frac{dP}{dX} = \frac{3(1+\alpha)}{2}\left[1-\lambda_D\left(1-\exp\left(\frac{-2}{\lambda_D}\right)\right)\right] \tag{5.2}$$

and

$$\begin{aligned} U(Y) = &-\exp\left[-\frac{1-Y}{\lambda_D}\right]-\alpha\exp\left(-\frac{1+Y}{\lambda_D}\right)+ \\ &\frac{3(Y^2-1)(1+\alpha)}{4}\left[1-\lambda_D\left(1-\exp\left(-\frac{2}{\lambda_D}\right)\right)\right]-\frac{(\alpha-1)Y}{2}+\frac{(\alpha+1)}{2} \end{aligned} \tag{5.3}$$

The corresponding expressions for the core flow (when one assumes slip boundary conditions) are:

$$\frac{dP}{dX} = \frac{3(1+\alpha)}{2} \tag{5.4}$$

and

$$U^c(Y) = \frac{(\alpha+1)}{4}(3Y^2-1)+\frac{1-\alpha}{2}Y\ . \tag{5.5}$$

Clearly, in the limit of $\lambda_D \to 0$, (5.2) and (5.3) reduce to (5.4) and (5.5). Fig. 4 depicts the velocity profiles obtained with equations (5.3) and (5.5) when α=1 (Fig. 4a) and α=-1 (Fig. 4b). With the exception of thin boundary layers of $0(\lambda_D)$, the approximate core solution is in excellent agreement with the exact one. Fig. 4b also depicts the velocity profile in the boundary layer next to Y=-1. For better visibility, the coordinates were stretched. The slender core solution that we

derived in this section will assist us in assessing the accuracy of the two-dimensional solution for the flow field in a finite-length cavity.

6. STEADY ELECTRO-OSMOTIC FLOW IN FINITE ASPECT-RATIO CAVITIES

The solution given in section 5 is valid only far away from the sidewalls. In this section, we compute the flow field in a finite aspect-ratio cavity with non-uniform, slowly varying ($\frac{1}{\zeta}\frac{d\zeta}{dX} << 1$) zeta potentials along the top and bottom walls (Y=±1). Based on the analysis of section 4, we use the electro-osmotic velocities as the slip boundary conditions at Y=±1. The time-independent, dimensionless Stokes equation is

$$\left.\begin{aligned} \nabla^2 \vec{V} &= \nabla P \\ \nabla \cdot \vec{V} &= 0 \end{aligned}\right\} \tag{6.1}$$

It is convenient to introduce the stream function Ψ such that $U = \frac{\partial \Psi}{\partial Y}$ and $V = -\frac{\partial \Psi}{\partial X}$. The streamfunction satisfies the biharmonic equation

$$\nabla^4 \Psi = 0 \tag{6.2}$$

with the boundary conditions:

$$\left.\begin{aligned} U(X,\pm 1) &= \frac{\partial \Psi}{\partial Y}(X,\pm 1) = U^{\pm}(X) \\ V(X,\pm 1) &= \Psi(X,\pm 1) = 0 \\ U(\pm h, Y) &= \Psi(\pm h, Y) = 0 \\ &\textit{and} \\ V(\pm h, Y) &= \frac{\partial \Psi}{\partial X}(\pm h, Y) = 0 \end{aligned}\right\} \tag{6.3}$$

In the above, h=L/H is the cavity's aspect ratio.

The biharmonic equation (6.2) can be readily solved with various numerical methods. We choose to solve (6.2) analytically since we need an accurate (and compact solution) to compute the trajectories of passive tracers under quasi-static, time-periodic fluctuations in the zeta potential (section 7).

Without loss of generality, it is convenient to decompose the problem into the four subproblems:

$$\Psi = \Psi_{EE} + \Psi_{EO} + \Psi_{OE} + \Psi_{OO} \tag{6.4}$$

In the above, the first subscript indicates whether the function is even (E) or odd (O) in X. The second subscript indicates whether the function is even (E) or odd (O) in Y. Accordingly, the boundary conditions for the various subproblems are:

$$U^{\pm}_{EE}(X) = \frac{1}{4}\left[U^{+}(X) + U^{+}(-X) + U^{-}(X) + U^{-}(-X)\right] \tag{6.5}$$

$$U^{\pm}_{EO}(X) = \pm\frac{1}{4}\left[U^{+}(X) + U^{+}(-X) - U^{-}(X) - U^{-}(-X)\right] \tag{6.6}$$

$$U^{\pm}_{OE}(X) = \frac{1}{4}\left[U^{+}(X) - U^{+}(-X) + U^{-}(X) - U^{-}(-X)\right] \tag{6.7}$$

$$U^{\pm}_{OO}(X) = \pm\frac{1}{4}\left[U^{+}(X) - U^{+}(-X) - U^{-}(X) + U^{-}(-X)\right] \tag{6.8}$$

Typically, the biharmonic equation in rectangular geometry is solved analytically with either biorthogonal 'Papkovich-Fadle' eigenfunctions [23-26] or the method of superposition [27]. When the boundary conditions are not smooth, Fourier series exhibit slow convergence due to the Gibbs phenomenon. It is easier, however, to accelerate the rate of convergence of the series when using the superposition method. For the even-odd case, Meleshko [17, 28] demonstrated that it is possible to achieve very accurate results while retaining just a few terms in the modified (accelerated) series. Following and extending Meleshko, we obtain the three

flow fields: Ψ_{EE}, Ψ_{OO} and Ψ_{OE}. We outline the derivation below and specify the modifications that are needed to accommodate the EE, OO, and OE cases.

EVEN ON X AND EVEN ON Y (Ψ_{EE})

We further decompose Ψ_{EE} into two components

$$\Psi_{EE}(X,Y) = \Psi_{EE}^{XY}(X,Y) + \Psi_{EE}^{ab}(X,Y), \tag{6.9}$$

where

$$\Psi_{EE}^{XY}(X,Y) = \sum_{m=1}^{M} \frac{(-1)^m}{\alpha_m} r_m p_m^e(Y) \cos(\alpha_m X) - h \sum_{\ell=1}^{L} \frac{(-1)^\ell}{\beta_\ell} s_\ell q_\ell^e(X) \sin(\beta_\ell Y), \tag{6.10}$$

and Ψ_{EE}^{ab} has a similar structure to Ψ_{EE}^{XY} with the coefficients r_m and s_l being replaced with the constants a and b. In the above, $M \to \infty$, $L \to \infty$,

$$\alpha_m = \frac{2m-1}{2h}\pi, \qquad \beta_\ell = \ell\pi, \tag{6.11}$$

$$p_m^e(Y) = \coth(\alpha_m)\frac{\sinh(\alpha_m Y)}{\sinh(\alpha_m)} - Y\frac{\cosh(\alpha_m Y)}{\sinh(\alpha_m)}, \tag{6.12}$$

and

$$q_\ell^e(X) = h\tanh(\beta_\ell h)\frac{\cosh(\beta_\ell X)}{\cosh(\beta_\ell h)} - X\frac{\sinh(\beta_\ell X)}{\cosh(\beta_\ell h)}. \tag{6.13}$$

The individual terms of the series (6.10) satisfy the biharmonic equation and the impermeability (Ψ=0) boundary condition. The first Fourier series (with the coefficients r_m) in 6.10 can represent any tangential velocity along |Y|=1. Likewise, the second Fourier series (with the coefficients s_ℓ) can represent any tangential velocity along the sidewalls |X|=h. The series

Ψ_{EE}^{ab} is designed to mimic the dominating singularities of $U^+(X)$ so that they do not hamper the rate of convergence of the series Ψ_{EE}^{XY}.

By taking the normal derivatives of Ψ_{EE} and requiring that the resulting series approximate the slip-velocity $U^+(X) = U^-(X)$ at |Y|=1 and the nonslip condition at |X|=h in the sense of weighted residuals, one obtains an infinite set of algebraic equations for the coefficients r_m and s_ℓ of the form:

$$\left.\begin{aligned} r_m\Delta_1(\alpha_m) + \sum_{\ell=1}^{\infty} s_\ell J(m,\ell,1) = F_m \\ s_\ell h\Delta_2(\beta_\ell h) - \sum_{m=1}^{\infty} r_m J(m,\ell,0) = G_\ell \end{aligned}\right\}, \tag{6.14}$$

where

$$J(m,\ell,k) = \frac{4\alpha_m^{k+1}\beta_\ell^{2-k}}{(\alpha_m^2+\beta_\ell^2)^2} \tag{6.15}$$

$$\Delta_1(\xi) = \frac{\xi}{\sinh^2(\xi)} - \coth(\xi), \qquad \Delta_2(\xi) = \tanh(\xi) + \frac{\xi}{\cosh^2(\xi)} \tag{6.16}$$

$$F_m = -a\Delta_1(\alpha_m) - b\sum_{\ell=1}^{\infty} J(m,\ell,1) + \alpha_m U_m \tag{6.17}$$

$$G_\ell = -bh\Delta_2(\beta_\ell h) + a\sum_{m=1}^{\infty} J(m,\ell,0) \tag{6.18}$$

and

$$U_m = \frac{(-1)^m}{h}\int_{-h}^{h} U^+(X)\cos(\alpha_m X)dX\,. \tag{6.19}$$

The series on the RHS of the equations are summed-up in terms of tri-gamma functions (Ψ', Abramowitz and Stegun [29]).

$$\sum_{\ell=1}^{\infty} J(m,\ell,1) = \frac{\alpha_m i}{\pi^2}\left[\Psi'(1+\frac{\alpha_m i}{\pi}) - \Psi'(1-\frac{\alpha_m i}{\pi})\right] \tag{6.20}$$

$$\sum_{m}^{\infty} J(m,\ell,0) = \frac{h^2\beta_\ell i}{A^2\pi^2}\left[\Psi'(\frac{1}{2}+\frac{h\beta_\ell i}{A\pi}) - \Psi'(\frac{1}{2}-\frac{h\beta_\ell i}{A\pi})\right] \tag{6.21}$$

In the above, A=1 when the summation is over all integer m-values and A=2 when the summation is over either odd or even m-values. $i = \sqrt{-1}$. The system of algebraic equations (6.14) with *a=b=0* can be truncated and solved for the coefficients r_m and s_ℓ. Kantorovich & Krylov [27] have shown that the resulting series is, indeed, convergent. Unfortunately, when the function $U^+(X)$ is not continuous, the rate of convergence may be quite slow. It is possible, however, to accelerate the rate of convergence by removing the dominant singularities. In other words, we wish to accelerate the rate of decay of the RHS of equations (6.14) as m and ℓ increase. This is done by choosing the arbitrary coefficients (*a*) and (*b*) in such a way as to increase the rate of decay of the RHS of the algebraic equations. The infinite sums in (6.17) and (6.18) are represented in terms of tri-gamma functions [17, 29]. By requiring that to the leading order, (6.17) and (6.18) are equal to zero (i.e., F_m=0 and G_ℓ=0), one can solve for *a* and *b*.

Here we will consider only the special case of uniform ζ potentials along the top and bottom boundaries (i.e., $U^+(X)=U^-(X)=U^+$ and $U_m=-\frac{2U^+}{\alpha_m h}$). Other velocity distributions can be handled in a similar way. Following the process described above, we obtain

$$a = \frac{2\pi^2 U^+}{h(\pi^2-4)}, \quad \text{and} \quad b = \frac{4\pi U^+}{h(\pi^2-4)}. \tag{6.22}$$

The truncated equations (6.14) with the above values of a and b and with the infinite sums on the RHS replaced with tri-gamma functions are solved for r_m and s_l. Next, we expand $p_m^e(Y)$ and

$q_\ell^e(X)$ into geometric series, exchange the order of summation, and sum-up the resulting inner series (Oberhettinger [30]) to obtain:

$$\Psi_{EE}^{ab}(X,Y) = aS_a(X,Y) - bhS_b(X,Y), \tag{6.23}$$

where

$$S_a(X,Y) = \sum_{m=1}^{\infty} \frac{(-1)^m}{\alpha_m} p_m^e(Y)\cos(\alpha_m X) = \sum_{v=0}^{\infty} \{S_1(X, v_1 - Y) - S_1(X, v_1 + Y)\} \tag{6.24}$$

$$S_b(X,Y) = \sum_{\ell=1}^{\infty} \frac{(-1)^\ell}{\beta_\ell} q_\ell^e(X)\sin(\beta_\ell Y) = \sum_{v=0}^{\infty} (-1)^v \{S_2(Y, v_1 h + X) + S_2(Y, v_1 h - X)\} \tag{6.25}$$

$$v_1 = 2v+1 \tag{6.26}$$

$$S_1(\xi,\eta) = -\frac{\eta h}{\pi}\arctan\left[\frac{\cos(\frac{\pi\xi}{2h})}{\sinh(\frac{\pi\eta}{2h})}\right] \tag{6.27}$$

and

$$S_2(\xi,\eta) = -\frac{\eta}{\pi}\arctan\left[\frac{\sin(\pi\xi)}{e^{\pi\eta} + \cos(\pi\xi)}\right] \tag{6.28}$$

The resulting series converges rapidly, and as few as M=L=5 terms are sufficient to obtain the desired precision. Additional details on the rate of convergence will be provided later in the paper.

ODD ON X AND ODD ON Y (Ψ_{OO})

The boundary conditions in this case satisfy $U^{\pm}(X) = -U^{\pm}(-X)$ and $U^{+}(X) = -U^{-}(X)$. As before, we decompose Ψ_{OO} into two components:

$$\Psi_{OO}(X,Y) = \Psi_{OO}^{XY}(X,Y) + \Psi_{OO}^{ab}(X,Y) \tag{6.29}$$

The first term, Ψ_{OO}^{XY}, is further decomposed into a sum of two Fourier series,

$$\Psi_{OO}^{XY}(X,Y)=\sum_{m=1}^{\infty}\frac{(-1)^m}{\alpha_m}r_m p_m^o(Y)\sin(\alpha_m X)-h\sum_{\ell=1}^{\infty}\frac{(-1)^\ell}{\beta_\ell}s_\ell q_\ell^o(X)\cos(\beta_\ell Y), \qquad (6.30)$$

where

$$\alpha_m=\frac{m}{h}\pi\ , \qquad \beta_\ell=\frac{(2\ell-1)}{2}\pi\ , \qquad (6.31)$$

$$\left.\begin{aligned} &p_m^o(Y)=\tanh(\alpha_m)\frac{\cosh(\alpha_m Y)}{\cosh(\alpha_m)}-Y\frac{\sinh(\alpha_m Y)}{\cosh(\alpha_m)},\\ &\textit{and}\\ &q_\ell^o(X)=h\coth(\beta_\ell h)\frac{\sinh(\beta_\ell X)}{\sinh(\beta_\ell h)}-X\frac{\cosh(\beta_\ell X)}{\sinh(\beta_\ell h)}. \end{aligned}\right\} \qquad (6.32)$$

Each term of the series (6.30) satisfies the biharmonic equation and the impermeability (Ψ=0) boundary conditions. By taking the normal derivatives of Ψ_{OO} at the sides |Y|=1 and |X|=h and taking inner products with the test functions $\sin(\alpha_m X)$ and $\cos(\beta_\ell Y)$, we obtain an infinite set of algebraic equations for the coefficients r_m and s_ℓ:

$$\left.\begin{aligned} &r_m\Delta_2(\alpha_m)-\sum_{\ell=1}^{\infty}s_\ell J(m,\ell,1)=-a\Delta_2(\alpha_m)+b\sum_{\ell=1}^{\infty}J(m,\ell,1)+\alpha_m U_m\\ &s_\ell h\Delta_1(\beta_\ell h)+\sum_{m}^{\infty}r_m J(m,\ell,0)=-bh\Delta_1(\beta_\ell h)-a\sum_{m}^{\infty}J(m,\ell,0) \end{aligned}\right\} \qquad (6.33)$$

In the above,

$$U_m=\frac{(-1)^{m-1}}{h}\int_{-h}^{h}U^+(X)\sin(\alpha_m X)dX \qquad (6.34)$$

By studying the asymptotic behavior of the series in the RHS of equation (6.33), one can determine the coefficients *a* and *b* so as to force the RHS of the algebraic equations to decay rapidly.

Here we will consider only the special case:

$$U^+(X) = -U^-(X) = -U^+ \qquad when \quad X < 0$$
$$U^+(-X) = -U^-(-X) = U^+ \qquad when \quad X > 0$$

Accordingly,

$$U_m = \begin{cases} \dfrac{4U^+}{\alpha_m h}, & odd \quad m \\ 0 \quad , & even \quad m \end{cases} \tag{6.35}$$

Witness that the RHS of equation (6.33) is different for odd and even m. Consequently, we split r_m into odd (r_m^o) and even (r_m^e). Equation (6.33) becomes

$$\left.\begin{aligned} & r_m^o \Delta_2(\alpha_m) - \sum_{\ell=1}^{\infty} s_\ell J(m,\ell,1) = -a^o \Delta_2(\alpha_m) + b\sum_{\ell=1}^{\infty} J(m,\ell,1) + \frac{4U^+}{h} \\ & r_m^e \Delta_2(\alpha_m) - \sum_{\ell=1}^{\infty} s_\ell J(m,\ell,1) = -a^e \Delta_2(\alpha_m) + b\sum_{\ell=1}^{\infty} J(m,\ell,1) \\ & s_\ell h \Delta_1(\beta_\ell h) + \sum_{odd \quad m}^{\infty} r_m^o J(m,\ell,0) + \sum_{even \quad m}^{\infty} r_m^e J(m,\ell,0) = \\ & -bh\Delta_1(\beta_\ell h) - a^o \sum_{odd \quad m}^{\infty} J(m,\ell,0) - a^e \sum_{even \quad m}^{\infty} J(m,\ell,0) \end{aligned}\right\}. \tag{6.36}$$

As before, the series on the RHS are summed up in terms of tri-gamma functions (equations 6.20 and 6.21). The coefficients a^e, a^o, and b are chosen so as to render to the leading order the RHS of the equations zero:

$$a^e = \frac{8U^+}{h(\pi^2 - 4)}, \quad a^o = \frac{4(\pi^2 - 2)U^+}{h(\pi^2 - 4)}, \quad \text{and} \quad b = \frac{4\pi U^+}{h(\pi^2 - 4)}. \tag{6.37}$$

Below, we list the main results and omit details.

$$\Psi_{OO}^{ab}(X,Y) = a^o S_a^o(X,Y) + a^e S_a^e(X,Y) - bhS_b(X,Y), \tag{6.38}$$

$$S_a^o(X,Y)=\sum_{odd\ m=1}^{\infty}\frac{(-1)^m}{\alpha_m}p_m^o(Y)\sin(\alpha_m X)=\sum_{v=0}^{\infty}(-1)^v\{S_3^o(X,v_1-Y)+S_3^o(X,v_1+Y)\}, \tag{6.39}$$

$$S_a^e(X,Y)=\sum_{even\ m=2}^{\infty}\frac{(-1)^m}{\alpha_m}p_m^o(Y)\sin(\alpha_m X)=\sum_{v=0}^{\infty}(-1)^v\{S_3^e(X,v_1-Y)+S_3^e(X,v_1+Y)\}, \tag{6.40}$$

$$S_b(X,Y)=\sum_{\ell=1}^{\infty}\frac{(-1)^\ell}{\beta_\ell}q_\ell^o(X)\cos(\beta_\ell Y)=\sum_{v=0}^{\infty}\{S_4(Y,v_1h-X)-S_4(Y,v_1h+X)\}, \tag{6.41}$$

$$S_3^o(\xi,\eta)=-\frac{\eta h}{2\pi}\arctan\left[\frac{\sin(\frac{\pi\xi}{h})}{\sinh(\frac{\pi\eta}{h})}\right] \tag{6.42}$$

$$S_3^e(\xi,\eta)=\frac{\eta h}{2\pi}\arctan\left[\frac{\sin(\frac{2\pi\xi}{h})}{e^{\frac{2\pi\eta}{h}}-\cos(\frac{2\pi\xi}{h})}\right], \tag{6.43}$$

and

$$S_4(\xi,\eta)=-\frac{\eta}{\pi}\arctan\left[\frac{\cos(\pi\xi/2)}{\sinh(\pi\eta/2)}\right]. \tag{6.44}$$

ODD ON X AND EVEN ON Y (Ψ_{OE})

The boundary conditions in this case are $U^{\pm}(X)=-U^{\pm}(-X)$ and $U^{+}(X)=U^{-}(X)$. As before, we write stream function Ψ_{OE} as the sum of $\Psi_{OE}^{XY}(X,Y)$ and $\Psi_{OE}^{ab}(X,Y)$. Ψ_{OE}^{XY} is decomposed into two Fourier series:

$$\Psi_{OE}^{XY}(X,Y)=\sum_{m=1}^{\infty}\frac{(-1)^m}{\alpha_m}r_m p_m^e(Y)\sin(\alpha_m X)-h\sum_{\ell=1}^{\infty}\frac{(-1)^\ell}{\beta_\ell}s_\ell q_\ell^o(X)\sin(\beta_\ell Y), \tag{6.45}$$

where

$$\alpha_m = \frac{m}{h}\pi \quad \text{and} \quad \beta_\ell = \ell\pi \,. \tag{6.46}$$

Each term of series (6.45) satisfies the biharmonic equation and the impermeability (Ψ=0) boundary conditions. By taking the normal derivatives of Ψ_{OE} at the sides |Y|=1 and |X|=h and taking the inner products with the test functions $\sin(\alpha_m X)$ and $\sin(\beta_\ell Y)$, we obtain an infinite set of algebraic equations for the coefficients r_m and s_ℓ:

$$\left.\begin{aligned} r_m \Delta_1(\alpha_m) + \sum_{\ell=1}^{\infty} s_\ell J(m,\ell,1) &= -a\Delta_1(\alpha_m) - b\sum_{\ell=1}^{\infty} J(m,\ell,1) + \alpha_m U_m \\ s_\ell h\Delta_1(\beta_\ell h) + \sum_{m=1}^{\infty} r_m J(m,\ell,0) &= -bh\Delta_1(\beta_\ell h) - a\sum_{m=1}^{\infty} J(m,\ell,0) \end{aligned}\right\} \tag{6.47}$$

where

$$U_m = \frac{(-1)^m}{h}\int_{-h}^{h} U^+(X)\sin(\alpha_m X)dX \tag{6.48}$$

By analyzing the asymptotic behavior of the RHS of equation (6.47), one can choose the coefficients *a* and *b* so as to accelerate the rate of decay of the RHS of (6.47).

Here we will consider only the special case of

$$\begin{aligned} U^+(X) = U^-(X) &= -U^+ \qquad when \quad X < 0 \\ U^+(-X) = U^-(-X) &= U^+ \qquad when \quad X > 0\,. \end{aligned}$$

Accordingly,

$$U_m = \begin{cases} -\dfrac{4U^+}{\alpha_m h}, & odd \quad m \\ 0\quad , & even \quad m \end{cases} \tag{6.49}$$

We split the coefficients r_m into odd and even. By suppressing the leading order of the RHS of the equations, we obtain the same coefficients a^e, a^o, and *b* listed in (6.37). As before,

$$\Psi_{OE}^{ab}(X,Y) = a^o S_a^o(X,Y) + a^e S_a^e(X,Y) - bhS_b(X,Y), \tag{6.50}$$

$$S_a^o(X,Y) = \sum_{odd\ m=1}^{\infty} \frac{(-1)^m}{\alpha_m} p_m^e(Y)\sin(\alpha_m X) = \sum_{v=0}^{\infty}\{S_3^o(X,v_1-Y) - S_3^o(X,v_1+Y)\}, \tag{6.51}$$

$$S_a^e(X,Y) = \sum_{even\ m=1}^{\infty} \frac{(-1)^m}{\alpha_m} p_m^e(Y)\sin(\alpha_m X) = \sum_{v=0}^{\infty}\{S_3^e(X,v_1-Y) - S_3^e(X,v_1+Y)\}, \tag{6.52}$$

and

$$S_b(X,Y) = \sum_{\ell=1}^{\infty} \frac{(-1)^\ell}{\beta_\ell} q_\ell^o(X)\sin(\beta_\ell Y) = \sum_{v=0}^{\infty}\{S_2(Y,v_1 h - X) - S_2(Y,v_1 h + X)\}. \tag{6.53}$$

The Accuracy of the Analytic Solutions

A number of researchers have studied Stokes flows driven by the motion of the upper and/or lower walls of closed, rectangular cavities. Gaskell et al. [26] compared the solutions obtained with Papkovich-Fadle eigenfunctions by Joseph and Sturges [23] and Shankar [25] with his own finite element calculations. Joseph and Sturges computed the series coefficients by utilizing a bi-orthogonal series to construct the infinite set of algebraic equations while Shankar determined the series coefficients by minimizing the "total square error." Gaskell concluded that when the number of terms in each series is sufficiently large (about 20), all the solutions were in good agreement in the cavity's interior. The analytical solutions were able to reproduce the boundary conditions with an average precision of 1% only when 200 terms were used. The maximum error at the boundary (in the corners' vicinity) was much larger due to the Gibbs phenomenon. Meleshko [17, 28] demonstrated that the method of superposition with series acceleration (that we used here) provides a much higher precision even at the point of singularity and even with only a relatively small number of terms in the Fourier series. For illustration

purposes, Fig. 5 depicts the deviation between the series sum and the boundary condition when M=L=5, h=1, and $U^+ = U^- = 1$. Clearly, the truncated series provides an excellent approximation (within 0.01%) even next to the singularities at |X|=h. In the cavity's interior, the precision of the analytic solution far exceeds its precision on the boundary. Fig.6 depicts the difference between the approximate core solutions $U_c(Y)$ (equation 5.5) and the two dimensional series solutions U(0,Y) as functions of Y when h=5, α=1 (Fig.6a), and α=-1 (Fig.6b). Both solutions are in excellent agreement. The small deviations may be attributed to *h* not being large enough.

7. TIME-INDEPENDENT, ELECTRO-OSMOTIC FLOWS IN A SQUARE CAVITY WITH DIFFERENT ZETA POTENTIAL DISTRIBUTIONS

In this section, we compute a few examples of flow fields in a square cavity (*h=1*) with different distributions of the zeta potentials along the cavity's walls. Fig. 7 depicts the streamlines when the ζ potential is uniform at the top and bottom walls, $U^+(X)=1$ and $U^-(X)=\alpha$, where α=-1 (a), α=1 (b), α=0 (c), and α=0.5 (d). When $\alpha < 0$, there is only one large eddy inside the cavity (Fig. 7a). When α=0 (Fig. 7c), in addition to the primary eddy, Moffatt [31] corner eddies are visible next to the bottom corners. When $\alpha>0$, the flow consists of a couple of counter-rotating eddies, whose size depends on α's magnitude. When $\alpha=\pm1$, the flow patterns are symmetric with respect to both the X=0 and Y=0 axes (Figs. 7a and b). When $\alpha\neq\pm1$, the symmetry with respect to the Y=0 axis is broken (Figs. 7c and d).

Figs. 8 and 9 depict the flow field when the ζ potential distribution is not uniform along the bottom and top walls. When $-h\leq X\leq -c/2$, $U^+=-1$ and $U^-=-\alpha$. When $c/2\leq X\leq h$, $U^+=1$ and $U^-=\alpha$. When $|X|<c$, $U=\zeta=0$. In the above, c ($>>\lambda_D$) is a small gap between the two adjacent electrodes.

In Fig. 9, we will demonstrate that small values of c have no significant effect on the flow topology as compared to the case of c=0. Therefore, in Fig. 8, we used c=0. Figs. 8a, b, c, and d correspond, respectively, to α= -1, 1, -0.5, and 0.5. By controlling the sign and magnitude of α, one can control the number of convective cells.

In Fig. 9, we examine the effect of the gap's width (c) on the flows' topology. In Figs. 9a and b, α=-1. In Figs. 9c and d, α=1. When c is small (c=0.1 in Figs. 9a and c), the flow field is similar to the case of c=0 (Figs. 8a and b). When c is large (c=0.5 in Figs. 9b and d), the flow cells appear to be skewed.

More complex patterns are shown in Fig. 10. In Fig. 10a, when $-h \le X < 0$, $U^+ = -U^- = -0.5$ and $0 < X \le h$, $U^+ = -U^- = 1$. In Fig. 10b, when $-h \le X < 0$, $U^+ = U^- = -0.5$, and when $0 < X \le h$, $U^+ = U^- = 1$. In Fig. 10c, when $-h \le X < 0$, $U^+ = -0.5$ and $U^- = 1$ and when $0 < X \le h$, $U^+ = 1$ and $U^- = -0.5$. In Fig. 10d, when $-h \le X < 0$, $U^+ = -0.5$ and $U^- = -1$, and when $0 < X \le h$, $U^+ = 1$ and $U^- = 0.5$. By controlling the relative magnitudes of the wall's ζ potential distribution, one can generate various flow patterns as well as reduce the symmetry of the flow patterns.

8. CHAOTIC ADVECTION INDUCED BY ELECTRO-OSMOSIS

So far, we have demonstrated that electro-osmosis can be used to induce complicated flow patterns in a closed cavity. These flows are, however, highly regular. In the absence of diffusion trace particles will follow the streamlines with no transport occurring transverse to the streamlines. In this section, we demonstrate that by appropriate time modulation of the ζ potential, one can induce chaotic advection. To this end, we choose two basic flow patterns, A and B say, and maintain flow field type A for a time interval $0 < t < T/2$, and then switch to flow field type B for the time interval $T/2 < t < T$. Subsequently, the process is repeated. We assume that

the Reynolds number is small and that the zeta potential alternations are sufficiently slow that the flow is quasi-static and the instantaneous flow field is given by the steady-state solution of the Stokes equation. This approximation has been widely used in the case of mixing problems at very low Reynolds numbers [19, 32-35]. For example, when studying a magnetohydrodynamic stirrer, Yi, Qian, & Bau [35] found that as long as St$\leq$1, the predictions of the quasi-static theory were in good agreement with computational results that accounted for the inertia term and with experimental observations.

When the flow field alternates between patterns A and B, the instantaneous flow field is given by:

$$\Psi(X,Y,t) = f_A(t)\Psi_A(X,Y) + f_B(t)\Psi_B(X,Y), \tag{8.1}$$

where

$$f_A(t) = \begin{cases} 1 & kT < t < kT + \dfrac{T}{2} \\ 0 & kT + \dfrac{T}{2} < t < (k+1)T \end{cases} \tag{8.2}$$

and

$$f_B(t) = \begin{cases} 0 & kT < t < kT + \dfrac{T}{2} \\ 1 & kT + \dfrac{T}{2} < t < (k+1)T \end{cases} \tag{8.3}$$

In the above, k=0,1,2,… is an integer, and the resulting flow field is periodic in time with periodicity T. Functions f(t) that provide a more gradual time-wise change will only modify the "effective" time interval T_i without changing the qualitative nature of the flow.

The motion of a passive tracer particle can be computed by solving the kinematic equations:

$$\left.\begin{aligned}\frac{dX}{dt} &= f_A(t)\frac{\partial \Psi_A(X,Y)}{\partial Y} + f_B(t)\frac{\partial \Psi_B(X,Y)}{\partial Y} \\ \frac{dY}{dt} &= -f_A(t)\frac{\partial \Psi_A(X,Y)}{\partial X} - f_B(t)\frac{\partial \Psi_B(X,Y)}{\partial X}\end{aligned}\right\} \tag{8.4}$$

with the initial conditions

$$X(0) = X_0, \qquad Y(0) = Y_0 \tag{8.5}$$

We compute the particle's trajectory by integrating equation (8.4) using Matlab's 4th order Runge-Kutta algorithm.

One can imagine the trajectory that a passive tracer will follow when the flow fields are alternately switched from pattern A to pattern B. In the time interval $kT < t < kT + \frac{T}{2}$, the tracer will move along a segment of the curve described by $\Psi_A = Const.$ In the time interval $kT + \frac{T}{2} < t < (k+1)T$, the tracer will follow a segment of the curve described by $\Psi_B = Const.$ The net result is a zigzag path. When T is small, the particle trajectory will coincide with a path traced by the superposition of patterns A and B. When T is relatively large, the zigzag path will cover most of the cross-sectional area, thereby providing efficient stirring.

As already noted by Aref [19] among others, equations 8.4 are a Hamiltonian system. The flow conserves area, and the phase space (x, y) coincides with the physical space. Although our treatment is valid only when T>>0, it is nevertheless instructive to examine the system in the limit of $T \to 0$. In this limit, the flow fields A and B superpose. By examining the various fixed points of the superposed field, one can obtain useful information on the advection patterns as T increases.

A few candidates for patterns A and B are depicted in Figs. 7 and 8. Many more can be envisioned, and we can choose any combination. The selection of the combination that leads to

the most efficient stirring is an interesting optimization problem that we do not address here. We restrict ourselves to two examples:

i. Mixing protocol A/B, where patterns A and B are depicted, respectively, in Figs. 7(a) and 8(b); and

ii. Mixing protocol ABCD, where patterns A and B are the same as in (i) above. Pattern C is similar to the one depicted in Fig. 7(b) with modified polarity ($U^+=U^-= -1$) and pattern D is depicted in Fig. 8(a). The time interval for each of the patterns is T/4.

Often stroboscopic images (Poincaré sections) are used as a diagnostic tool to determine the effectiveness of the stirring process. These images are obtained by integrating the kinematic equations and documenting the tracer's location at the end of each period. In other words, each image is a superposition of snapshots that depict the location of the tracer particle at times t=kT, where k=0, 1, 2, … When the pattern of points that emerges lies on a smooth curve, the motion is deemed to be regular and provides poor mixing. When a scattered pattern emerges, the motion is likely to be chaotic.

The combined flow field of protocol A/B is depicted in Fig. 11a in the limit of $T\rightarrow 0$. When the period $T\rightarrow 0$, the flow field is characterized by large outer eddies containing two sub-eddies separated by a saddle stagnation point. The flow field includes one hyperbolic and two elliptic fixed points.

When T=0, the system is autonomous and integrable. When T>0, the system may no longer be integrable. As T increases, chaotic behavior arises both because of the disruption of the hyperbolic fixed point and the perturbation of the tori. In the first instance, the stable and unstable manifolds of the hyperbolic point (in the Poincare section) intersect transversely infinitely many times to form a homoclinic tangle and a "hyperbolic mixing region".

Additionally, according to the Poincare-Birkhoff theorem [36], the tori with rational period ratios (Γ/T) will deform significantly and form a "petal" structure that leads in the Poincare section to the formation of a sequence of new hyperbolic (saddle) and elliptic fixed points. Like the original hyperbolic point, these newly formed hyperbolic points will give rise to chaotic behavior. In summary, in our system, there are two interacting mechanisms that lead to chaotic advection. This process is illustrated in Fig. 12 when T=0.6. The figure depicts the stroboscopic image (Poincare section) of passive tracer particles' trajectories initially inserted at (-0.4, 0), (-0.25, -0.5), (-0.25, -0.4), (-0.1, -0.2), (-0.1, -0.3), (0, 1.0e-3), (0.1, 0.2), (0.1, 0.3), (0.25, 0.4), (0.25, 0.5), and (0.45, 0). Witness the emergence of the chaotic region resulting from the homoclinic tangle and the formation of new hyperbolic and elliptic points.

As the period T is further increased, the passive tracer particle inserted at (X0, Y0)=(0, 0.01) strays away from the “regular path”, and it circulates from the upper right region to the bottom left region (Fig. 11b). As T is further increased to T=2 (Fig. 11c), the fraction of the cavity’s area visited by the tracer also increases. Figs. 11b and 11c indicate the presence of isolated regions bound by KAM surfaces through which the tracer particles do not pass. As T increases, the size of these isolated islands decreases, and they are barely visible in Fig. 11d (T=8). Given the symmetries of each of the flow patterns, the appearance of the isolated islands is not surprising [37]. Presumably, more effective stirring would be achieved by minimizing the symmetries of flow patterns A and B. Alternatively, the KAM surfaces might disappear if one were to adopt a quasi-periodic alternation protocol instead of the periodic one that we used here. In Fig. 11d (T=8), the chaotic region spreads to cover most of the cavity and nearly wipes out the regular regions indicating an effective stirring process.

Fig. 13 depicts the trajectories of passive tracers when protocol ABCD is used. Fig. 13a depicts the superimposed flow field ($T\rightarrow 0$), and Figs.13b and 13c depict the trajectories of a particle initially positioned at location (x, y)=(0.3, 0.3) when T=2 and T=4, respectively. As in Fig. 11, as T increases, so does the complexity in the cavity.

In order to better illustrate the stirring process, like Aref [19], we inserted a square material blob (i.e., dye) of edge size 0.1 with 10^4 particles, initially centered at (0, 0), and we tracked the deformation of the material blob. Figs. 14 and 15 depict, respectively, the evolution of the blob for the protocols of A/B and ABCD when T=8. In each case, we integrated the trajectories of 10^4 particles, initially uniformly distributed within the blob. The particles' trajectories were tracked for the time interval $0<t<20T$. These figures illustrate the blob's stretching and folding process. Ultimately, the fluid particles spread to cover almost the entire area of the cavity.

Although some of the basic flow patterns presented here are similar to the ones calculated in previous works on chaotic advection in cavity flows [38-40], the present study differs from the previous efforts in a number of ways. Prior workers used finite difference techniques to calculate the flow field. These calculations required a great amount of computer resources. In contrast, we derived quasi-analytical solutions for the flow field that provide a much better precision than the finite difference solutions with a relatively small computational effort, and do not require interpolation. In contrast to prior works, in which one or more of the stirrer's boundaries had to be set into motion, the proposed stirrer does not require any moving parts. Finally, local control of the zeta potential allows one to obtain a rich plethora of flow patterns that may not be feasible to realize by other means.

In most cases of electroosmotic flows, the surface roughness exceeds the thickness of the electric double layer. Although the surface roughness distorts locally the electric and flow fields next to the boundary, it has little effect on the bulk flow [41].

9. CONCLUSION

In this paper, we have studied electro-osmotic flows in cavities in which the zeta potential along the cavities walls varies both spatially and temporally. Asymptotic and quasi-analytic solutions for the flow field were derived, respectively, for the cases of the slender and finite aspect ratio rectangular cavities. In the latter case, solutions have been derived for various canonical cases. By accelerating the rate of convergence of the series, we were able to obtain highly accurate solutions while maintaining just a few terms in the series. These series solutions have a clear advantage over finite difference and finite element solutions, particularly when one desires to track the progression of passive tracer particles; not only do they provide computational economy, they also save the need for interpolation, which would be required in finite difference and finite elements simulations. Non-uniform, wall zeta potentials lead to the formation of complex flow patterns. By temporally varying the wall's zeta potential, one can obtain chaotic advection that may provide efficient stirring. The stirring efficiency is somewhat compromised due to the appearance of islands. However, the ability to locally control the zeta potential allows one to induce a plethora of flow patterns and minimize the presence of symmetries in the flow. Furthermore, the islands might be eliminated with the use of aperiodic alternations of the flow patterns. Since the electro-osmotic stirrer does not require any moving parts, it is particularly suitable for applications in microfluidic systems.

ACKNOWLEDGMENTS

The work described in this paper was supported, in part, by DARPA (Dr. Anantha Krishnan, Program Director) through a grant (N66001-01-C-8056) to the University of Pennsylvania. An abbreviated version of the paper was presented at the 2002 ASME International Mechanical Engineering Congress & Exposition, New Orleans, Louisiana, November 17-22, 2002 (paper # IMECE2002-33763).

REFERENCES

[1] K.F. Jensen, Microchemical Systems: Status, Challenges, and Opportunities, *AICHE J.*, 45(1999),2051-2054

[2] R. Langer, Biomaterials: Status, Challenges, and Perspectives, *AICHE J.*, 46(2000), 1286-1289

[3] H. A. Stone and S. Kim, Microfluidics: Basic Issues, Applications, and Challenges, *AICHE J.*, 47 (2001), 1250-1254.

[4] R.F. Probstein, *Physiochemical Hydrodynamics* (John Wiley & Sons: NY, 1994).

[5] P. Dutta and A. Beskok, Analytical solution of combined eloectoossmotic/pressure driven flows in two-dimensional straight channels: Finite Debye layer effects, *Analytical Chemistry* 73(2001), 1979-1986.

[6] J.L. Anderson and W.K. Idol, Electroosmosis through pores with nonuniformly charged walls, Chemical Engineering Communications 38 (1985), 93-106.

[7] A. Ajdari, Electroosmosis on Inhomogeneously Charged Surfaces, *Physical Review Letters*, 75(1995), 755-758

[8] A. Ajdari, Generation of Transverse Fluid Currents and Forces by an Electric Field: Electro-osmosis on Charged-modulated and undulated Surfaces, *Physical Review E*, 53(1996), 4996-5005

[9] A. Ajdari, Pumping liquids using asymmetric electrode arrays, Physical Review E 61(2000), R45-48.

[10] S.Z. Qian and H.H. Bau, A chaotic electroosmotic stirrer, Analytical Chemistry 74 (2002), 3616-3625.

[11] D. Erickson and D. Q. Li, Influence of surface heterogeneity on electrokinetically driven microfluidic mixing**,** Langmuir, 18 (2002), 1883-1892.

[12] A.D. Stroock, M. Weck, D.T. Chiu, W.T.S. Huck, P.J.A. Kenis, R.F. Ismagilov, G.M. Whitesides, Patterning Electroosmotic Flow with Patterned Surface Charge, *Physical Review Letters*, 84 (2000), 3314-3317.

[13] C. S. Lee, W.C. Blanchard, and C.T. Wu, Direct control of the electroosmosis in capillary zone electrophoresis by using an external electric field. *Analytical Chemistry,* 58 (1990), 1550-1552.

[14] R.B.M. Schasfoort, S. Schlautmann, J. Hendrikse, and A. Van den Berg, Field-Effect Flow Control for Microfabricated Fluidic Networks, *Science*, 286 (1999), 942-945

[15] J.S. Buch, P-C. Wang, D.L. DeVoe, C.S. Lee, Field-effect flow control in a polydimethylsiloxane-based microfluidic system, Electrophoresis, 22(2001), 3902-3907.

[16] J. Moorthy , C. Khoury, J.S. Moore, and D.J. Beebe, Active control of electroosmotic flow in microchannels using light, *Sensors and Actuators B-Chemical* ,75(2001), 223-229.

[17] V.V. Meleshko, Steady Stokes flow in a rectangular cavity, *Proc. R. Soc. Lond. A*, 452 (1996), 1999-2022

[18] A. Souvaliotis, S.C. Jana, and J.M. Ottino, Potentialities and limitations of mixing simulations, *AIChE J.,* 41 (1995), 1605-1621.

[19] H. Aref, Stirring by chaotic advection, *Journal of Fluid Mechanics*, 143(1984), 1-21

[20] A.W. Adamson, *Physical Chemistry of Surfaces* (Wiley, 1990), 5th edition.

[21] J.L. Anderson, Colloid Transport by Interfacial Forces**,** *Annual Review of Fluid Mechanics,* 21(1989), 61- 99

[22] J. Kevorkian and J.D. Cole, *Perturbation Methods in Applied Mathematics* (Springer, 1981).

[23] D.D. Joseph and L.D. Sturges, Convergence of biorthogonal series for biharmonic and flow edge problems, *SIAM J. Appl. Math.,* 34(1978), 7-26

[24] L.D. Sturges, Stokes-flow in a two-dimensional cavity with moving end walls, *Physics Fluids,* 29 (1986), 1731-1734.

[25] P.N. Shankar, The eddy structure in stokes-flow in a cavity, *J. Fluid Mech.*, 250(1993), 371-383.

[26] P.H. Gaskell, M.D. Savage, J.L. Summers, and H.M. Thompson, Stokes flow in closed, rectangular domains, *Applied Mathematical Modeling*, 22(1998), 727-743.

[27] L.V. Kantorovich and V.I. Krylov, *Approximate Methods of Higher Analysis* (Interscience Publishers, Inc., NY., 1958).

[28] V. V. Meleshko and A. M. Gomilko, Infinite systems for a biharmonic problem in a rectangular, *Proc. R. Soc. Lond. A*, 453(1997), 2139-2160

[29] M. Abramowitz and I.A. Stehum, *Handbook of Mathematical Functions* (New York,1972)

[30] F. Oberhettinger, *Fourier Expansions* (Academic Press, NY., 1973).

[31] H. K. Moffatt, Viscous and resistive eddies near a sharp corner, *J. Fluid Mech.*, 18 (1964), 1-18.

[32] H. Aref and S. Balachandar, Chaotic Advection in Stokes Flow, *Physics Fluids*, 29(1986), 3515-3521

[33] J. Chaiken, C.K. Chu, M. Tabor, and Q.,M. Tan, Lagrangian Turbulence and Spatial Complexity in Stokes Flow, *Physics Fluids*, 30(1987), 687-694

[34] S.Z. Qian, J.Z. Zhu, and H.H. Bau, A stirrer for magnetohydrodynamically controlled minute fluidic networks, *Physics of Fluids*,14 (2002), 3584-2592.

[35] M. Yi, S. Qian, and H.H. Bau, A magnetohydrodynamic chaotic stirrer, *Journal of Fluid Mechanics*, 468(2002), 153-177

[36] J., M. Ottino, *The Kinematics of Mixing: Stretching, Chaos, and Transport* (Cambridge, 1989).

[37] J. G. Franjione, C-W Leong, and J. M. Ottino, Symmetries within chaos-a route to effective mixing, *Phys. Fluids A,* 1 (1989), 1772-1783.

[38] C.W. Leong and J.M. Ottino, Experiments on mixing due to chaotic advection in a cavity, *Journal of Fluid Mechanics,* 209(1989),463-499

[39] S.C. Jana, G. Metcalfe, and J.M. Ottino, Experimental and computational studies of mixing in complex stokes flows-the vortex mixing flow and multicellular cavity flows, *Journal of Fluid Mechanics,* 269(1994),199-246

[40] S. C. Jana and J. M. Ottino, Chaos-enhanced transport in cellular flows, *Phil. Trans. Roy. Soc. Lond.*, 338 (1992), 519-532

[41] Y. Hu, C. Werner, and D. Li, Electrokinetic transport through rough microchannels, Analytical Chemistry, 75(2003), 5747-5758

LIST OF CAPTIONS

1. A rectangular cavity equipped with two electrodes (|X|=h) in contact with the liquid. These electrodes induce a uniform electric field in the x-direction. Additional electrodes (A_i, i=1,2,3, and 4) are embedded in the upper and lower walls of the cavity beneath the surface. These electrodes are used to control the walls' zeta potential.
2. Velocity profiles for various pressure gradients when α=1 (a) and α= -1 (b). $\lambda_D = 0.01$.
3. Velocity profiles for different zeta potential ratios (α) when dP/dX=-2 (a) and dP/dX=2 (b). $\lambda_D = 0.01$.
4. Velocity profiles within a closed cavity. α=1(a) and α=-1(b). The solid line and symbols (o) correspond, respectively, to the exact and approximate core solutions. In (b), the horizontal upper and vertical RHS scales are blown up to facilitate a better appreciation of the boundary layer structure (dash line). $\lambda_D = 0.01$.
5. The difference between the computed velocities at the boundary and the exact values. M=L=5, h=1, and $U^+_{EE}(X) = 1$.
6. The difference between the slender cavity's one-dimensional solution and the solution of the biharmonic equation when h=5, α=1 (a) and α= -1 (b).
7. Streamline patterns for electro-osmotic flow with uniform ζ potentials at the top and bottom surfaces. U^+=1 and U^-=α, h=1, and M=L=5. (a) α= -1, (b) α= 1, (c) α= 0, and (d) α= 0.5
8. Streamline patterns for electro-osmotic flow with non-uniform zeta potentials at the top and bottom surfaces.h=1 and M=L=5. When -h≤X≤0, U^+= -1 and U^-= -α. When 0≤X≤h, U^+= 1 and U^-=α. (a) α= -1, (b) α= 1, (c) α= -0.5, and (d) α= 0.5

9. The effect on the streamline patterns of the width of the gap (c) between two zones with different ζ potentials. When $-h \le X \le -c$, $U^+ = -1$ and $U^- = -\alpha$. When $c \le X \le h$, $U^+ = 1$ and $U^- = \alpha$, and when $|X| < c$, $U^+ = U^- = 0$. (a) c=0.1 and α=-1, (b) c=0.5 and α=-1 , (c) c=0.1 and α=1, and (d) c=0.5 and α=1. h=1 and M=L=5.

10. Streamline patterns for the electro-osmotic flow when there are non-uniform zeta potentials at the top and bottom surfaces. h=1 and M=L=5. When $-h \le X \le 0$, $U^+ = -0.5$ and $U^- = \alpha_1$. When $0 \le X \le h$, $U^+ = 1$ and $U^- = \alpha_2$. (a) $\alpha_1 = 0.5$, $\alpha_2 = -1$, (b) $\alpha_1 = -0.5$, $\alpha_2 = 1$, (c) $\alpha_1 = 1$, $\alpha_2 = -0.5$, (d) $\alpha_1 = -1$, $\alpha_2 = 0.5$

11. Stroboscopic images of the flow field induced by protocol AB when T=0 (a); T=1(b); T=2 (c); and T=8 (d). (X_0, Y_0)=(0,0.01), $0 < t < 3000T$, h=1, and M=L=5

12. Stroboscopic images of the flow field induced by protocol AB when T=0.6. (X_0, Y_0)= (-0.4, 0), (-0.25, -0.5), (-0.25, -0.4), (-0.1, -0.2), (-0.1, -0.3), (0, 1.0e-3), (0.1, 0.2), (0.1, 0.3), (0.25, 0.4), (0.25, 0.5), and (0.45, 0). h=1 and M=L=5.

13. Stroboscopic images of the flow field induced by protocol ABCD when T=0 (a); T=2(b); and T=4 (c). (X_0, Y_0)=(0.3,0.3), $0 < t < 3000T$, h=1, and M=L=5.

14. The deformation of a material blob of edge size 0.1 initially (t=0) centered at (0,0) when T=8. Stirring protocol AB. (a) t=0; (b) t=2T; (c) t=4T; (d) t=6T; (e) t=7T; (f) t=8T; (g) t=10T; (h) t=12T; and (i) t= 20T

15. The deformation of a material blob of edge size 0.1, initially (t=0) centered at (0,0), when T=8. Stirring protocol ABCD. (a) t=0; (b) t=1T; (c) t=2T; (d)t=3T; (e)t=4T; (f) t=5T; (g)t=6; (h) t=7T; and (i) t= 20T

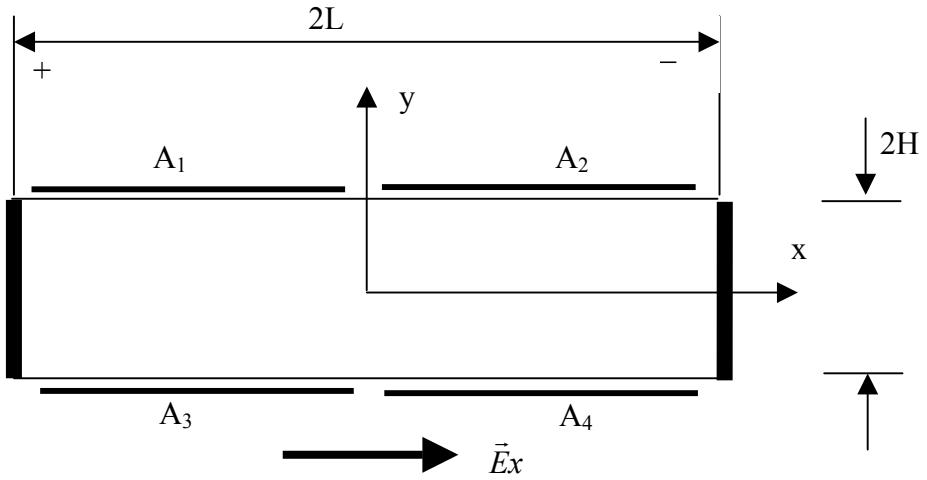

Fig. 1: A rectangular cavity equipped with two electrodes (|X|=h) in contact with the liquid. These electrodes induce a uniform electric field in the x-direction. Additional electrodes (A_i, i=1,2,3, and 4) are embedded in the upper and lower walls of the cavity beneath the surface. These electrodes are used to control the wall zeta potential.

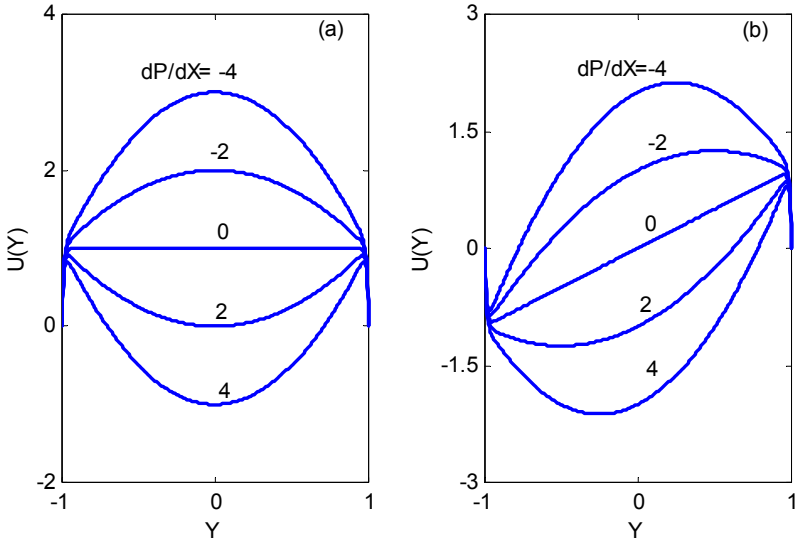

Fig. 2: Velocity profiles for various pressure gradients when α=1 (a) and α= -1 (b). $\lambda_D = 0.01$.

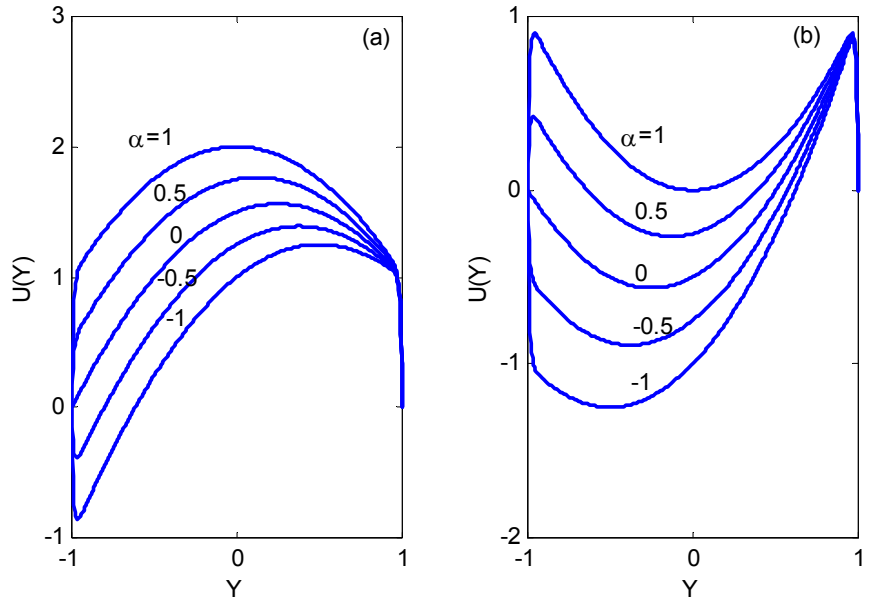

Fig. 3: Velocity profiles for different zeta potential ratios (α) when dP/dX=-2 (a) and dP/dX=2 (b). $\lambda_D = 0.01$.

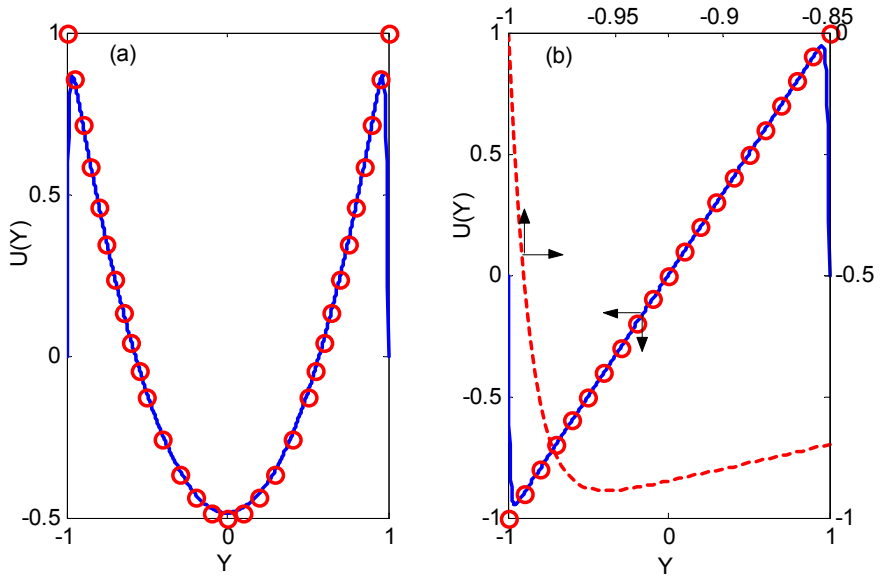

Fig. 4: Velocity profiles within a closed cavity. α=1(a) and α=-1(b). The solid line and symbols (o) correspond, respectively, to the exact and approximate core solutions. In (b), the horizontal upper and vertical RHS scales are blown up to facilitate a better appreciation of the boundary layer structure (dash line). $\lambda_D = 0.01$.

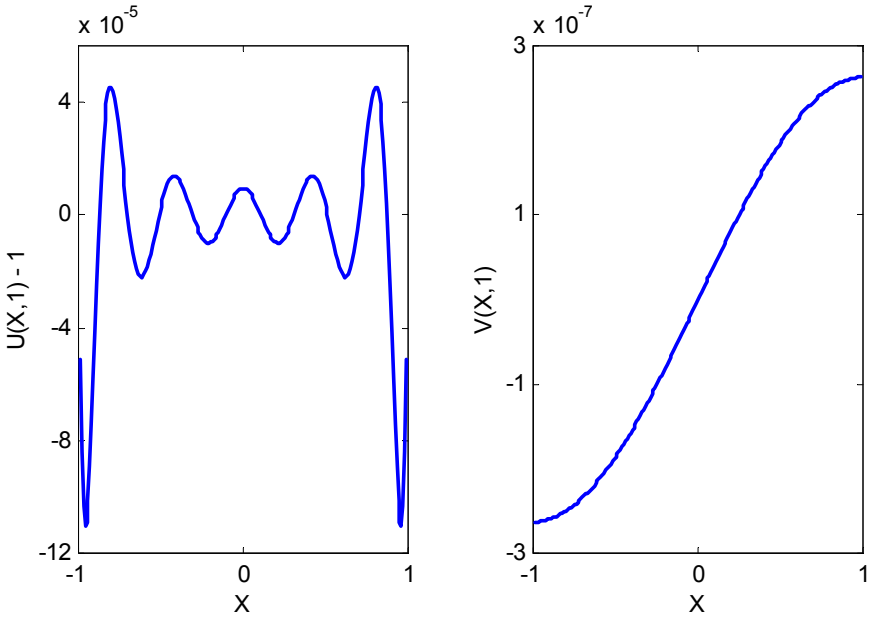

Fig. 5: The difference between the computed velocities at the boundary and the exact values. M=L=5, h=1, and $U^{+}_{EE}(X)=1$.

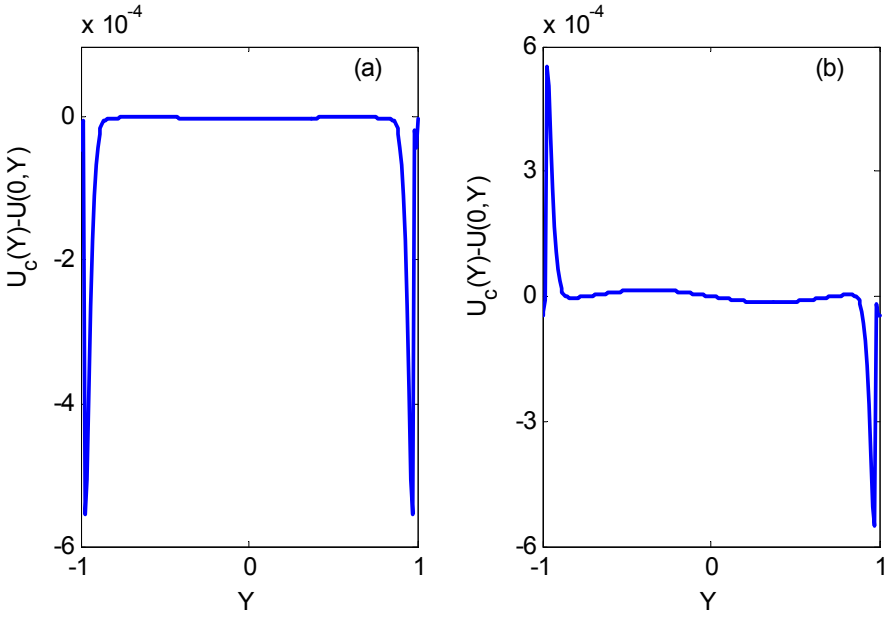

Fig. 6: The difference between the slender cavity's one-dimensional solution and the solution of the biharmonic equation when h=5, α=1 (a) and α= -1

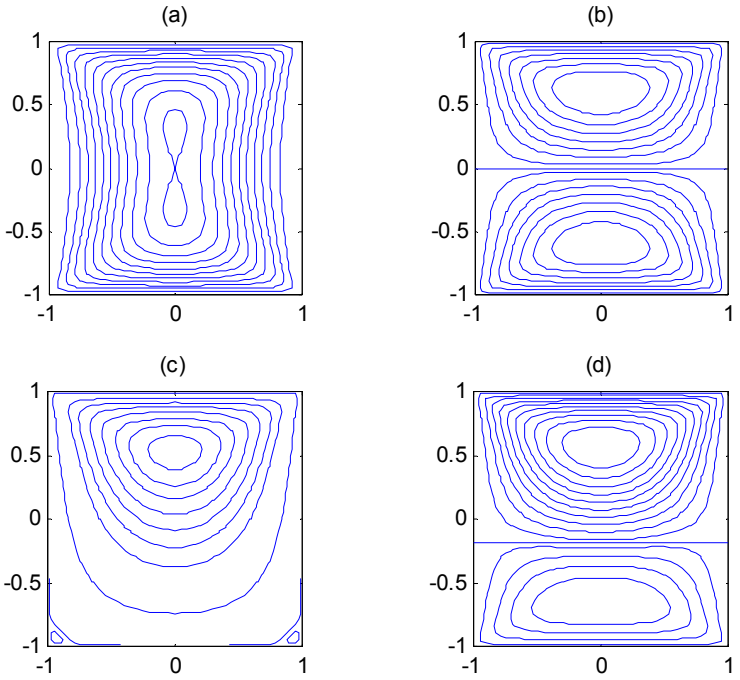

Fig. 7: Streamline patterns for electroosmotic flow with uniform ζ potentials at the top and bottom surfaces. U^+=1 and U^-=α. h=1 and M=L=5. (a) α= -1, (b) α= 1, (c) α= 0, and (d) α= 0.5

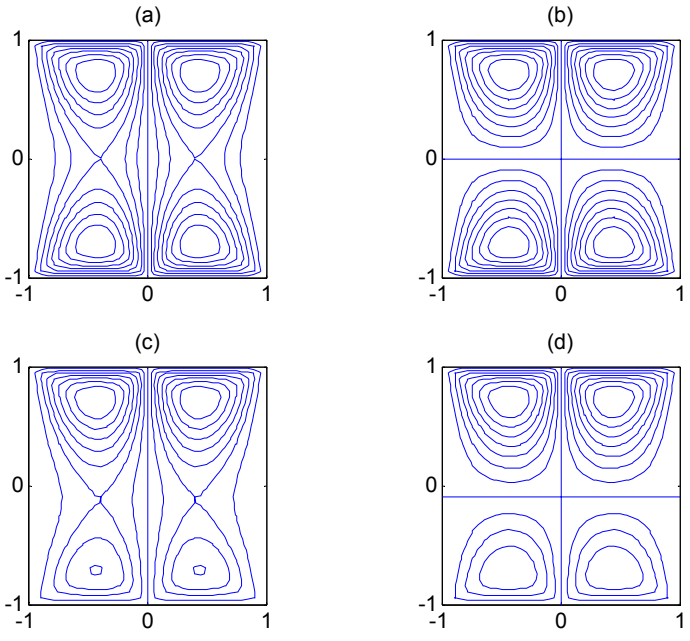

Fig. 8: Streamline patterns for electroosmotic flow with non-uniform zeta potentials at the top and bottom surfaces.h=1 and M=L=5. When -h≤X≤0, U^+= -1 and U^-= -α. When 0≤X≤h, U^+= 1 and U^-=α. (a) α= -1, (b) α= 1, (c) α= -0.5, and (d) α= 0.5

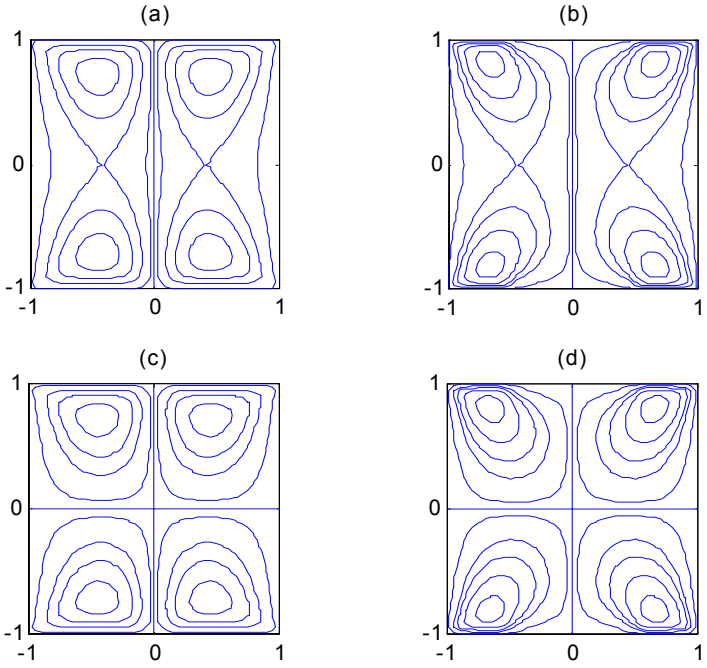

Fig.9: The effect of the gap width (c) between two zones of different ζ potentials on the streamline patterns. When $-h \le X \le -c$, $U^+ = -1$ and $U^- = -\alpha$. When $c \le X \le h$, $U^+ = 1$ and $U^- = \alpha$, and when $|X| < c$, $U^+ = U^- = 0$. (a) c=0.1 and $\alpha=-1$ (b) c=0.5 and $\alpha=-1$, (c) c=0.1 and $\alpha=1$, and (d) c=0.5 and $\alpha=1$. h=1 and M=L=5.

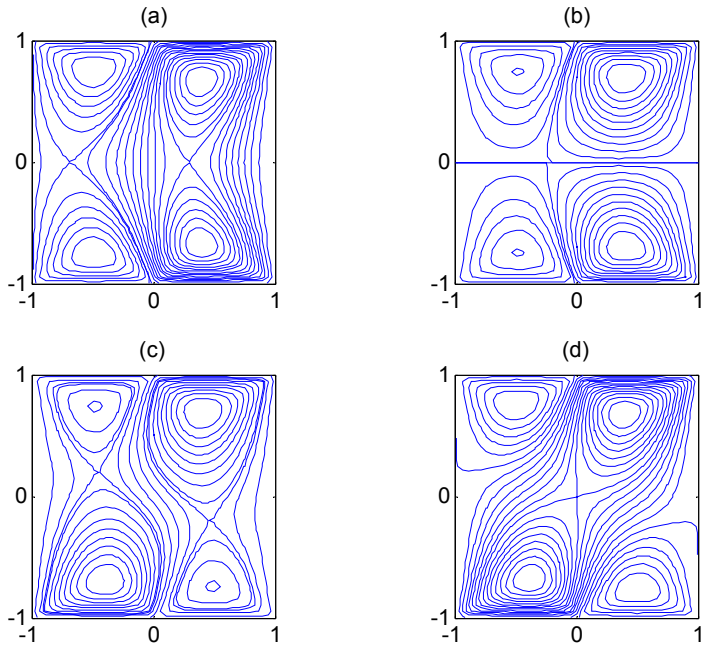

Fig. 10: Streamline patterns for the electroosmotic flow with non-uniform zeta potentials at the top and bottom surfaces. h=1 and M=L=5. When $-h \le X \le 0$, $U^+ = -0.5$ and $U^- = \alpha_1$. When $0 \le X \le h$, $U^+ = 1$ and $U^- = \alpha_2$. (a) $\alpha_1 = 0.5$, $\alpha_2 = -1$, (b) $\alpha_1 = -0.5$, $\alpha_2 = 1$, (c) $\alpha_1 = 1$, $\alpha_2 = -0.5$, (d) $\alpha_1 = -1$, $\alpha_2 = 0.5$

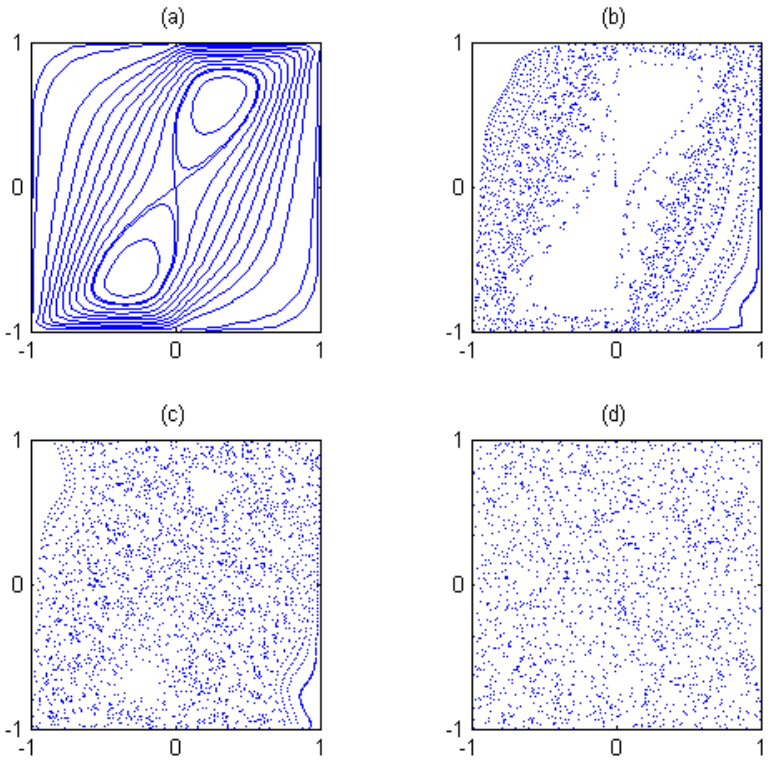

Fig. 11: Stroboscopic images of the flow field induced by protocol AB when T=0 (a); T=1(b); T=2 (c); and T=8 (d). $(X_0, Y_0)=(0,0.01)$, $0<t<3000T$, h=1, and M=L=5

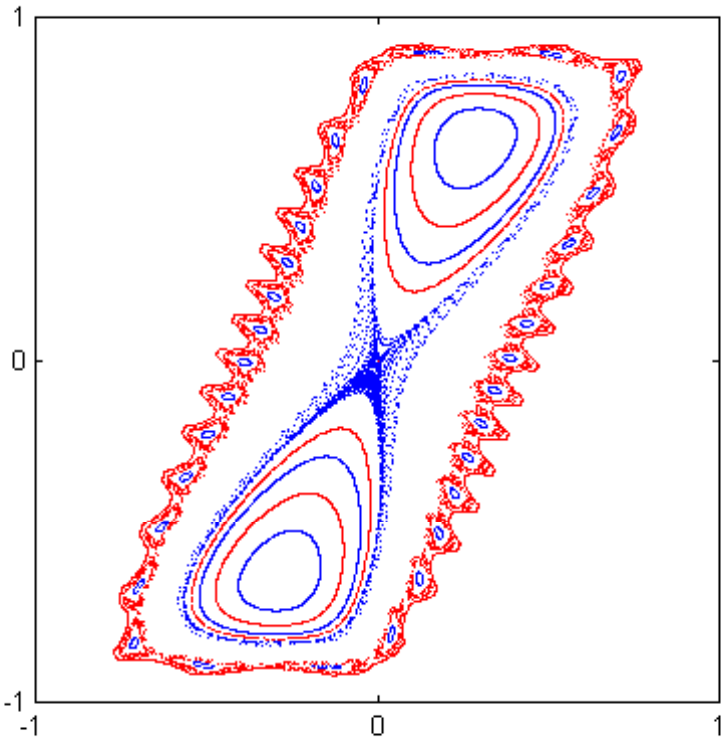

Fig. 12: Stroboscopic images of the flow field induced by protocol AB when T=0.6. (X_0, Y_0)= (-0.4, 0), (-0.25, -0.5), (-0.25, -0.4), (-0.1, -0.2), (-0.1, -0.3), (0, 1.0e-3), (0.1, 0.2), (0.1, 0.3), (0.25, 0.4), (0.25, 0.5), and (0.45, 0). h=1 and M=L=5.

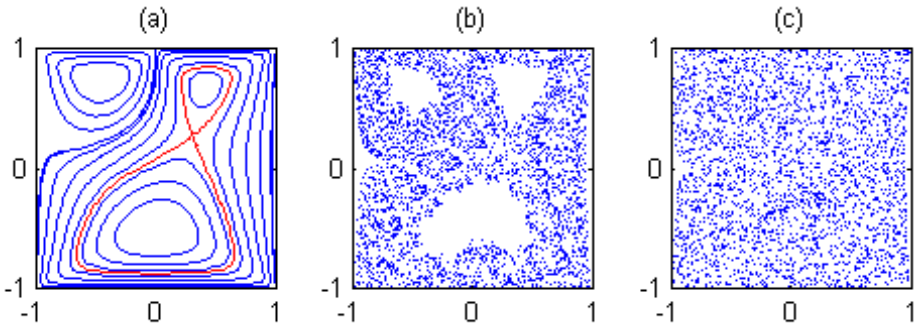

Fig. 13: Stroboscopic images of the flow field induced by protocol ABCD when T=0 (a); T=2(b); and T=4 (c). (X_0, Y_0)=(0.3,0.3), 0<t<3000T, h=1, and M=L=5.

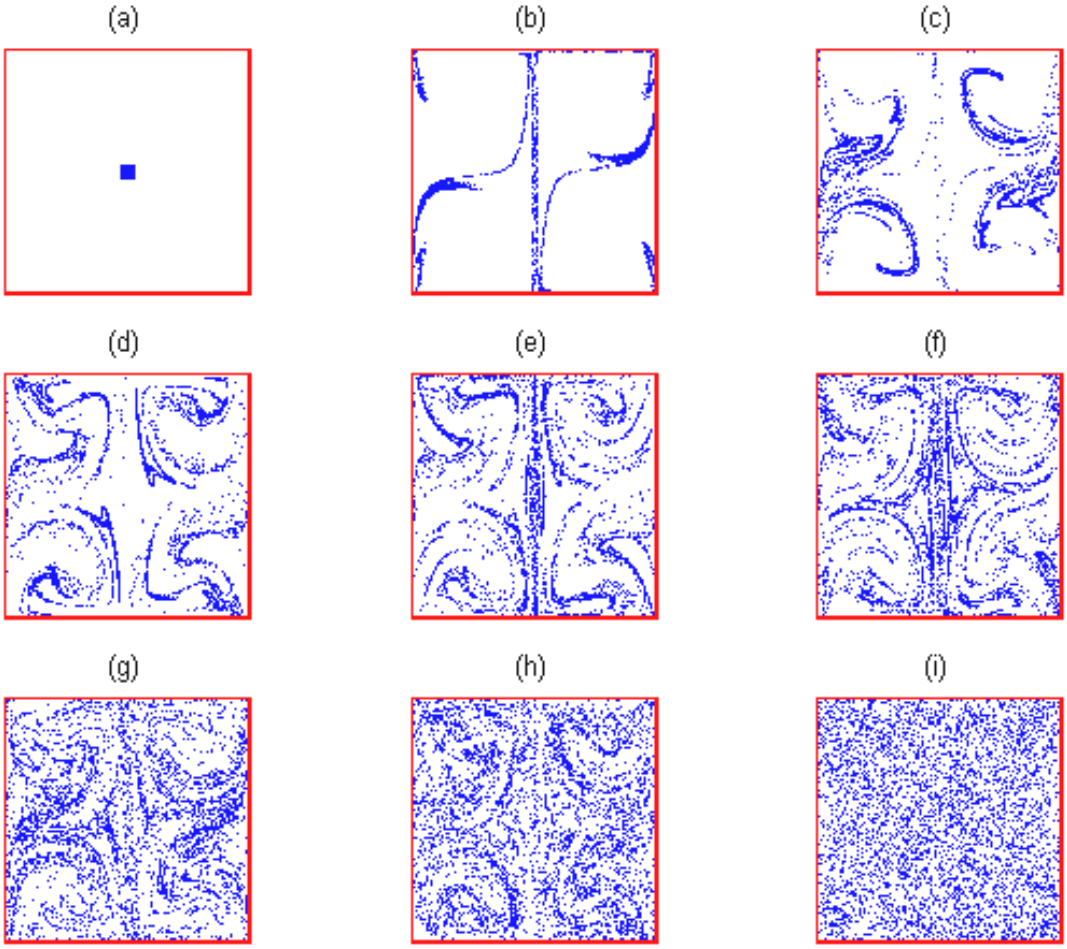

Fig. 14: The deformation of a material blob of edge size 0.1 initially (t=0) centered at (0,0) when T=8. Stirring protocol AB. (a) t=0; (b) t=2T; (c) t=4T; (d) t=6T; (e) t=7T; (f) t=8T; (g) t=10T; (h) t=12T; and (i) t= 20T

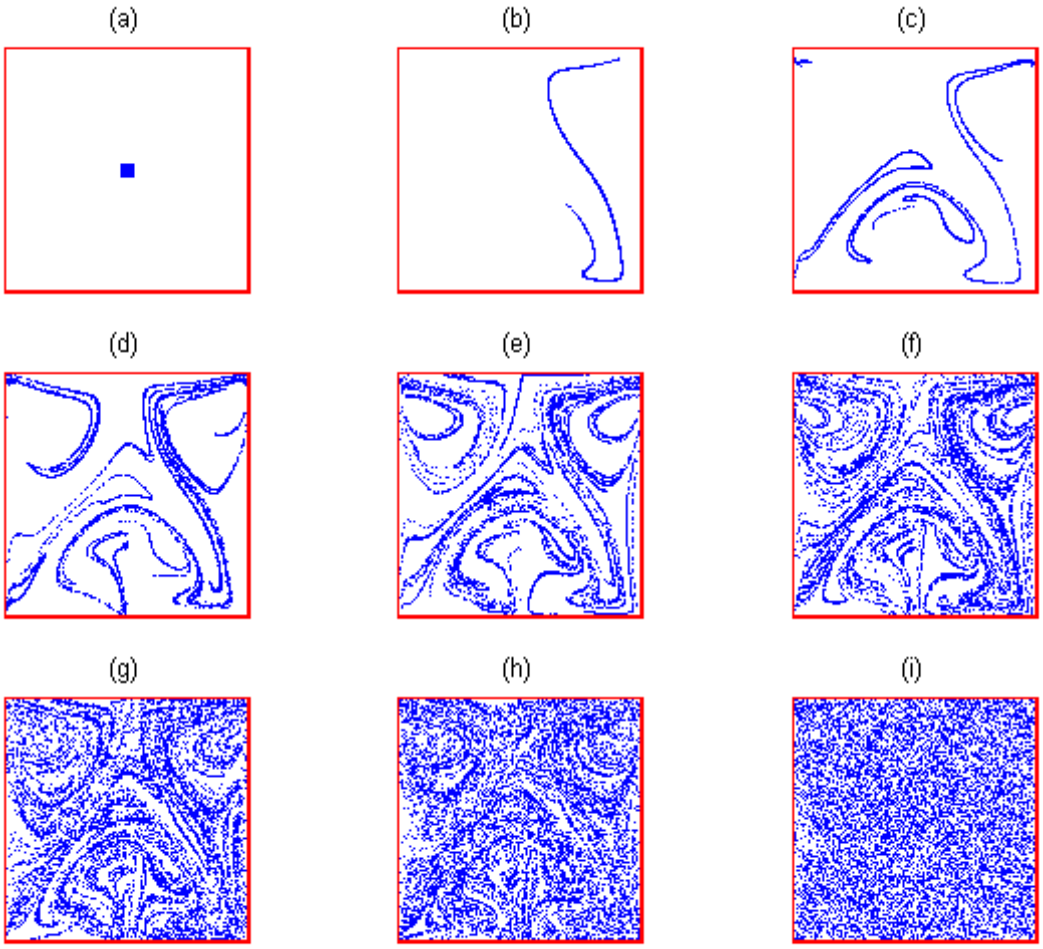

Fig.15: The deformation of a material blob of edge size 0.1 initially (t=0) centered at (0,0) when T=8. Stirring protocol ABCD. (a) t=0; (b) t=1T; (c) t=2T; (d)t=3T; (e)t=4T; (f) t=5T; (g)t=6; (h) t=7T; and (i) t= 20T